Exotic distributions of rigid unit modes in the reciprocal spaces of framework aluminosilicates

2007 J. Phys.: Condens. Matter 19 275209

(http://iopscience.iop.org/0953-8984/19/27/275209)

IOP PUBLISHING JOURNAL OF PHYSICS: CONDENSED MATTER

J. Phys.: Condens. Matter **19** (2007) 275209 (20pp) doi:10.1088/0953-8984/19/27/275209

Exotic distributions of rigid unit modes in the reciprocal spaces of framework aluminosilicates

Martin T Dove[1,3], Alexandra K A Pryde[1], Volker Heine[2] and Kenton D Hammonds[1]

[1] Department of Earth Sciences, University of Cambridge, Downing Street, Cambridge CB2 3EQ, UK
[2] Department of Physics, Cavendish Laboratory, J J Thomson Avenue, Cambridge CB3 0HE, UK

E-mail: mtd10@cam.ac.uk

Received 29 December 2006, in final form 2 January 2007
Published 1 June 2007
Online at stacks.iop.org/JPhysCM/19/275209

Abstract

Until recently it was assumed that rigid unit modes, defined as the zero-frequency solutions to the dynamical equations for an infinite framework of rigid corner-linked tetrahedra, were confined to a small set of normal modes with wavevectors on lines or planes of special symmetry in reciprocal space. Using a search method that explores the full three-dimensional reciprocal space, we have located rigid unit modes with wavevectors on exotic curved surfaces in reciprocal space for a range of silicate minerals. This has led to the realization that the crystal structures of these minerals contain rather more topological floppiness than had previously been realized. The origin of the exotic RUM surfaces remains to be understood.

(Some figures in this article are in colour only in the electronic version)

1. Introduction

This paper is part of a collection that has a strong focus on displacive phase transitions. For a displacive phase transition to occur, there needs to be an easy (i.e. with low energy cost) way for the parent structure to distort, which is related to the idea that a displacive phase transition is driven by a soft phonon. For some time our group in Cambridge has been exploring the question of why many framework materials—materials whose crystal structures are composed of infinite frameworks of corner-linked polyhedral groups of atoms—are unstable against displacive phase transitions. The most famous example is quartz, with a crystal structure that can be described in terms of corner-linked SiO_4 tetrahedra, but it appears that many materials of this type will display displacive phase transitions.

[3] Author to whom any correspondence should be addressed.

The origin of the displacive instability in quartz has a long history. It was recognized several years ago that the geometry of the framework allows for the easy mechanical instability that is associated with the phase transition [1]. This initial work was then developed by the Grenoble group [2–4], who considered the origin of structural instabilities from a lattice dynamical perspective. This was the inspiration that sparked the work of our group in Cambridge, in which we developed the concept of the rigid unit mode (RUM). RUMs are the normal modes of vibrations of a crystal containing linked polyhedra that propagate without causing any distortion of these polyhedra [5–7]. One of our first tasks was to develop a tool to compute all RUMs for any given structure [6, 8], which enabled us to explore the structural instabilities of a wide range of network silicates and aluminosilicates [7, 9].

Although the mechanical instability in quartz was well-established, it was not at all clear why so many framework structures could accommodate RUM instabilities. Some insight into this question is given by the application of the Thorpe–Phillips constraint analysis [11–13]. This is explored in detail elsewhere [5–7, 9]; the important point here is that structures composed of corner-linked tetrahedra have an exact balance between the number of constraints and the number of degrees of freedom. This means that such structures are balanced between being too rigid to support any RUMs and being floppy. In this scenario one expects there to be no RUMs in any structure. Thus for a RUM to exist with a particular wavevector, it is required that symmetry renders two of the topological constraints degenerate, leaving a net degree of freedom for that wavevector [6, 9]. From this, intuition led to the assumption that RUMs would be found only for special wavevectors, whether special points, along symmetry axes or on planes of symmetry in reciprocal space [6]. Thus the initial studies of RUMs in silicates were primarily concerned with RUMs on special lines and planes of wavevectors [9]. All aluminosilicate structures containing SiO_4 and AlO_4 tetrahedra linked into an infinite framework that were studied were found to have RUMs for some wavevectors [7], but structures containing octahedra as part of the framework frequently have no RUMs [10]. Also, it was found that when a material undergoes a displacive phase transition, there are more RUMs in the higher-symmetry phase [7]. On the other hand, most materials that contain structural octahedra do not contain RUMs [10], even if these are corner linked. The cubic perovskite phases are a notable exception; in this case symmetry plays a significant role in make some of the constraints degenerate, but the number of RUMs in these structures is small [6].

The discovery of complex curved surfaces of diffuse scattering in electron diffraction from the HP (hexagonal primitive) phase of tridymite, SiO_2 [14], which were shown to arise from RUMs with wavevectors on curved surfaces in reciprocal space [15], showed that RUMs are not confined to special wavevectors. Moreover, a study of the RUMs in the negative-thermal-expansion ceramic ZrW_2O_8 provided an example of a material where there are no RUMs on special wavevectors but with RUMs for wavevectors on a complex curved surface within the Brillouin zone [16]—although this material contains ZrO_6 octahedra, the balance between numbers of constraints and degrees of freedom is maintained by the WO_4 tetrahedra containing unlinked W–O bonds. These results have indicated the need to explore the whole of the Brillouin zone for RUMs, and clearly prompt the question of whether similar curved surfaces of RUM wavevectors exist in other framework structures.

The present paper addresses this question by investigating a representative selection of framework silicates and aluminosilicates. In the case of the aluminosilicates, the interstitial cations, e.g. potassium, sodium, etc, are ignored because it is the vibrational properties of the frameworks of rigid tetrahedra (representing the SiO_4 and AlO_4 units) that are of interest. In practice, these interstitial cations will tend to stiffen the framework slightly and reduce the oscillation amplitude of the RUMs. The distributions of RUMs lying on special wavevectors in the crystals investigated here have been reported previously [7]. The results of the present

search at general wavevectors include the discovery of a number of exotic curved surfaces of RUM wavevectors in these crystals, where both the number of RUM wavevectors and the complexity of their distribution in reciprocal space is surprising. The present work also includes comparisons of the RUM distributions for different phases related by a displacive phase transition.

2. Method of calculation

Rigid unit modes can be defined as the zero-frequency solutions to the dynamical equations for an infinite framework of rigid corner-linked tetrahedra with completely flexible linkages (i.e. no restoring forces associated with changing the linkage angles). An analytical approach was used by Vallade and co-workers [2, 4] to enumerate all the RUMs for β-quartz, but this analytical approach is not practical for general routine applications. Our approach is to use a numerical method based on our split-atom method [6]. The essence of this approach is to represent the rigid tetrahedra as individual rigid molecules, and to represent the atoms shared by two tetrahedra as a pair of atoms with the same positions, one for each tetrahedron, which we call the 'split atoms'. The split atoms are held together by a strong harmonic force. The dynamical equations for this model can be expressed in terms of standard molecular lattice dynamics, and the zero-frequency solutions are the rigid unit mode solutions. We have adapted a programme for the solution of the dynamical equations for the split-atom model, which is called CRUSH [6, 8], and is based upon a molecular lattice dynamics program. CRUSH will generate all the zero-frequency solutions for a given structure described as a framework of linked rigid units (not restricted to tetrahedra or corner-sharing) for any given wavevector.

To perform the searches for this study, the program CRUSH was modified to generate values of a pseudo-intensity for two- and three-dimensional grids of wavevectors. The pseudo-intensity was defined by

$$I(\mathbf{k}) = \sum_j \frac{1}{\omega_{j,\mathbf{k}}^2 + \Omega} \tag{1}$$

where $\mathbf{k}$ is the wavevector, $\omega_{j,\mathbf{k}}$ is the frequency of a phonon at the given value of $\mathbf{k}$ calculated by CRUSH, Ω is a small quantity chosen to prevent $I(\mathbf{k})$ diverging to infinity when there is a RUM at a given $\mathbf{k}$, and the sum is over all phonons (labelled by j) at a given $\mathbf{k}$. Therefore, for a wavevector at which there are n RUMs, $I(\mathbf{k}) \approx n\Omega^{-1}$. Where a RUM exists at a wavevector $\mathbf{k}_{\mathrm{RUM}}$, for a wavevector in reciprocal space close to $\mathbf{k}_{\mathrm{RUM}}$ but for which there is no RUM, the intensity will vary as $I(\mathbf{k}) \propto |\mathbf{k} - \mathbf{k}_{\mathrm{RUM}}|^{-2}$.

$I(\mathbf{k})$ simulates the results of a thermal diffuse scattering experiment in one sense, in that it has the correct dependence of phonon frequency [17], but it does not include the components associated with the structure factor and phonon eigenvector so the results obtained in the first Brillouin zone will be reflected over the rest of reciprocal space. This is different from the experimental situation where the pattern of the diffuse scattering is the same for all Brillouin zones, but the intensity of the diffuse scattering varies across the whole of reciprocal space.

The orthogonal grids of wavevectors used to generate the three-dimensional figures all used the same grid spacing. The spacing between neighbouring points was 0.001 $\mathrm{\AA}^{-1}$, generating 10^9 points per $\mathrm{\AA}^{-3}$. The value $\Omega = 0.001$ THz^2 was used, and the typical maximum value for the frequencies was $\omega_{\max} = 35$ THz (this value was controlled by the value of the force constant used in the split-atom method).

The RUM distributions are presented as three-dimensional contour plots in reciprocal space, which include perspective. The number of RUMs at a given wavevector is represented using the colour coding in the on-line version, with the colour key given in table 1. The section

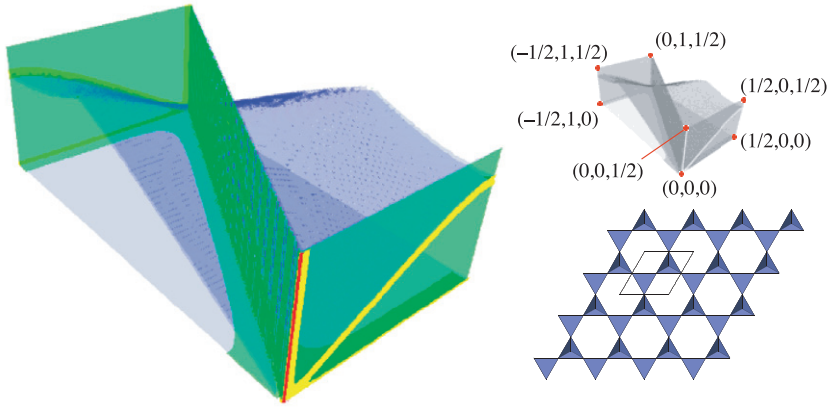

Figure 1. The distribution of RUM wavevectors in a section of reciprocal space for HP tridymite (the on-line version uses the colour code given in table 1). The upper small inset shows labels of specific points in reciprocal space to aid interpretation. The lower small inset shows a representation of the crystal structure; the space group for this phase is $P6_3/mmc$.

Table 1. The colour-coding used in the three-dimensional figures of RUMs in reciprocal space (on-line version only).

Colour	No. of RUMs
Blue	1
Green	2
Yellow	3
Red	4+

of reciprocal space presented for a particular crystal structure is dependent upon its Bravais lattice. In order to make the figures as clear as possible, these sections are the minimum necessary to include the set of symmetrically independent wavevectors. In each figure of the RUM distributions we label a smaller version with key points in reciprocal space, and we also show the associated crystal structure.

3. Tridymite, SiO_2

3.1. HP tridymite

The existence of a large number of different deformations of the ideal tridymite structure, i.e. different tridymite phases, is indicative of the high flexibility of this particular framework structure. Consequently, it is expected that there will be a large number of RUMs permitted by the structure, particularly in the higher-symmetry phases. Tridymite is the first example described here because of the earlier study prompted by the diffuse scattering in the electron diffraction measurements [15].

The RUMs for wavevectors of special symmetry have been tabulated by Hammonds *et al* [7], and are visible as planes and lines in figure 1. There is a (blue) plane covering the base of the box shape, which represents a single RUM for all wavevectors of the form $(\xi, \zeta, 0)$. There are two RUMs for all wavevectors $(\xi, 0, \zeta)$, which can be seen as the two ends of the (green) Z-shape rising out of the base of the box. The middle section of the Z-shape represents the two RUMs with wavevectors of the form $(0, \xi, \zeta)$. The $(\xi, \zeta, 0)$ and $(\xi, 0, \zeta)$ symmetry

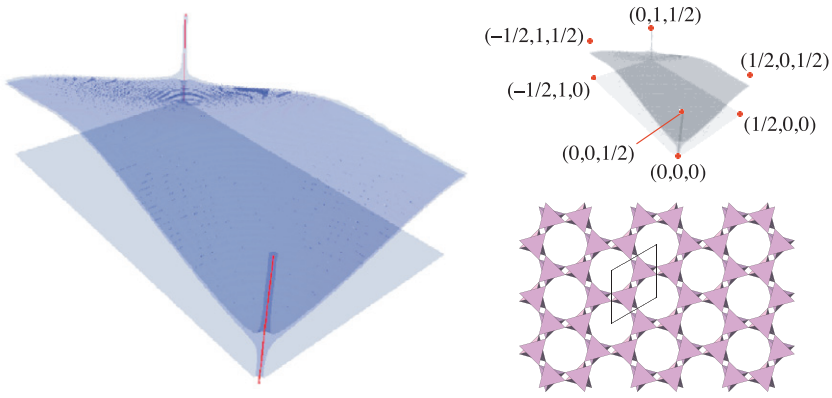

Figure 2. The distribution of RUM wavevectors in a section of reciprocal space for LHP tridymite (the on-line version uses the colour code given in table 1). The upper small inset shows labels of specific points in reciprocal space to aid interpretation. The lower small inset shows a representation of the crystal structure; the space group for this phase is $P6_322$.

planes intersect along the line $[\xi, 0, 0]^\star$, and along there are three RUMs, visible as a (yellow) line along the bottom of the front face of the box in figure 1. In fact the (green) Z end faces bleed slightly into the (blue) $(\xi, \zeta, 0)$ plane (the base of the box), indicating a lowering of the frequency of the second lowest phonon in the (blue) basal plane, as the (yellow) $[\xi, 0, 0]^\star$ lines are approached. A similar effect is seen around the line $[0, 0, \xi]^\star$, which is the intersection of the $(\xi, 0, \zeta)$ and $(0, \xi, \zeta)$ planes. In fact there are six RUMs along this line, and the yellow vertical lines in the green $(\xi, 0, \zeta)$ plane arise from a softening on approaching the $[0, 0, \xi]^\star$ line.

The feature revealed for the first time in its entirety by this search is the undulating blue surface between the $(\xi, \zeta, 0)$ and $(\xi, \zeta, \frac{1}{2})$ planes (the bottom and top faces of the box). The curved intersection of this undulating surface with the $(\xi, 0, \zeta)$ end face is the feature first observed in the electron diffraction study [14] and interpreted as RUMs [15]. The areas with a darker shade of blue are where the translucent undulating surface partially obscures the view of the RUM plane on the base of the box. A similar surface is found for the LHP phase (figure 2).

It is interesting to determine the nature of the lattice distortions caused by the RUMs with wavevectors along such unusual curves in reciprocal space. This was investigated by calculating the RUM eigenvectors, which describe the components of the RUM distortion in terms of the six degrees of freedom of each SiO_4 tetrahedron, for the RUMs on the curved sections in the $[\bar{1}, 1, 0]$ zone. It turns out that the amplitudes of the components in the RUM eigenvector are fairly constant along these curved loci. The predominant components the translation of the SiO_4 tetrahedra parallel to the **c** axis and the rotation of the tetrahedra about an axis parallel to the **a** axis. The eigenvector also includes small amounts of the other possible displacements, with the exception of rotations of the tetrahedra about an axis parallel to the z direction—the amplitude of these displacements is identically zero.

3.2. LHP (low hexagonal primitive) tridymite

Following the HP–LHP transition some of the RUMs in the HP phase are no longer RUMs in the LHP phase as a result of the reduction in symmetry of the crystal structure. This includes the RUMS on the Z planes noted above. A relatively large number of RUMs do remain, however, and their distribution is clearly related to that of the RUMs present in the HP phase (figure 2).

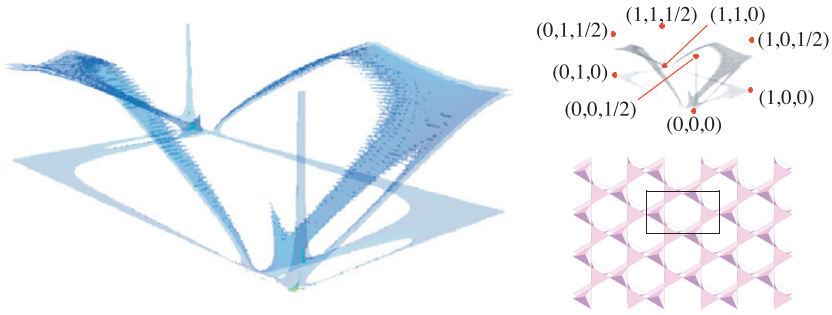

Figure 3. The distribution of RUM wavevectors in a section of reciprocal space for OC tridymite (the on-line version uses the colour code given in table 1). The upper small inset shows labels of specific points in reciprocal space to aid interpretation. The lower small inset shows a representation of the crystal structure; the space group for this phase is $C222_1$.

For wavevectors along the $[0, 0, \xi]^\star$ line, four of the previous six RUMs remain, and this is indicated by the (red) vertical line. The single RUM for wave vectors in the $(\xi, \zeta, 0)$ plane remains and so does the undulating blue surface of single RUMs, albeit slightly flattened in shape.

3.3. OC (orthorhombic C-centred) tridymite

The LHP–OC transition does not change the number of atoms in a primitive unit cell of the structure and so, despite the change from hexagonal to orthogonal coordinates, the section of reciprocal space presented in figure 3 is equivalent to the sections presented for HP and LHP tridymite (apart from very small scaling differences due to slight changes in the lattice parameters). The phase transition to OC tridymite results in an incomplete erosion of the (blue) undulating surface and the (blue) plane present for the LHP phase. The parts of these RUM surfaces which remain include the symmetry lines $[\xi, 0, 0]^\star$ and $[0, \xi, 0]^\star$. A single RUM also remains along the $[0, 0, \xi]^\star$ line, where there were four in the LHP phase.

3.4. OP (orthorhombic primitive) tridymite

The unit cell of the OP phase is a $3 \times 1 \times 1$ supercell of the conventional (i.e. C-centred) unit cell of the OC phase. It is therefore approximately six times the size of the OC primitive unit cell. The c axis remains unchanged and so there is no change in the $\mathbf{c}^\star$ dimension in reciprocal space. The relationship between the $\mathbf{a}^\star$ and $\mathbf{b}^\star$ section of reciprocal space presented for the OP phase and the sections presented for the other phases (which have hexagonal and C-centred structures) is shown schematically in figure 4. As a result of the changes in cell volume, the OP phase has six times as many phonons per wavevector than the other structures. This accounts for the observation from figure 5 that there still appears to be a large number of RUMs, despite the reduction in structural symmetry.

The distribution of RUM wavevectors for the OP phase (figure 5) is rather nebulous and it is not easy to see many clear features. A large number of wavevectors have one RUM, shown by the blue surfaces, and this includes the plane $(\xi, \zeta, 0)$. There are other small regions where the number of RUMs is two, the green areas, or even three, the yellow areas, e.g. on the $(\xi, \zeta, 0)$ plane and the $[\frac{1}{2}, 0, \xi]^\star$ line.

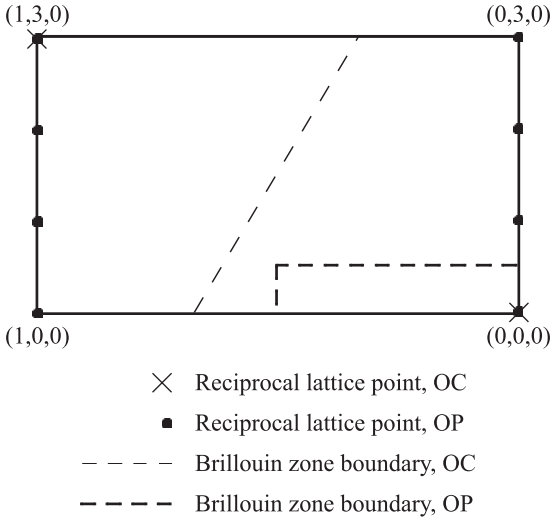

Figure 4. Comparison of the sections of reciprocal space presented for the HP, LHP and OC phases (thick solid rectangle) and OP tridymite (thick dashed inset). The indices of the reciprocal lattice points are given in the OP setting.

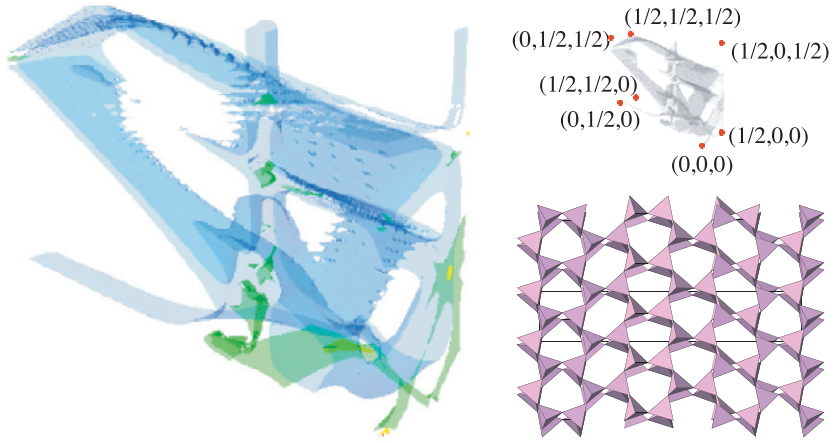

Figure 5. The distribution of RUM wavevectors in a section of reciprocal space for OP tridymite (the on-line version uses the colour code given in table 1). The upper small inset shows labels of specific points in reciprocal space to aid interpretation. The lower small inset shows a representation of the crystal structure; the space group for this phase is $P2_12_12_1$.

4. Tridymite derivatives

4.1. Kalsilite, $KAlSiO_4$

The crystal structure of kalsilite, which is shown in figure 6, has essentially the same network of tetrahedra as LHP tridymite, the main difference being that there are two sizes of tetrahedra due to the ordered arrangement of SiO_4 and AlO_4 tetrahedra. Kalsilite also contains interstitial cations, but these are not included in the calculations of the RUM spectrum. These cations will

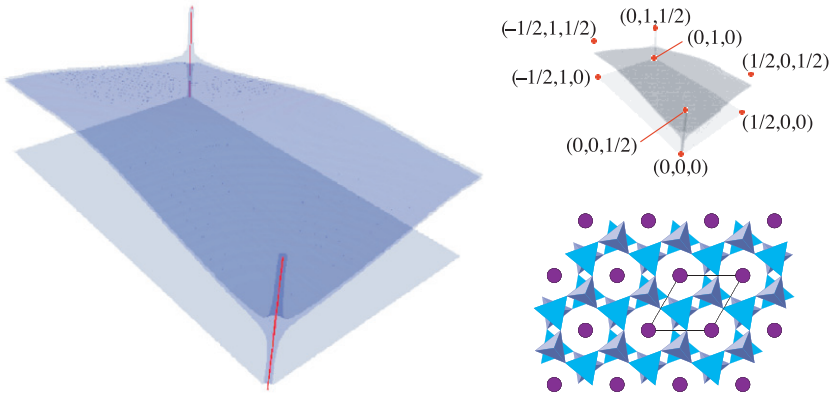

Figure 6. The distribution of RUM wavevectors in a section of reciprocal space for kalsilite (the on-line version uses the colour code given in table 1). The upper small inset shows labels of specific points in reciprocal space to aid interpretation. The lower small inset shows a representation of the crystal structure; the space group for this phase is $P6_3mc$.

tend to stiffen the framework and reduce the amplitude of oscillation of the RUMs, but will not affect the CRUSH calculations. Thus the RUM distribution as a whole is very similar to that for LHP tridymite, as can be seen by comparing figure 6 with figure 2. The (blue) plane which covers the base of the box in figure 6 represents a single RUM, which exists for all wavevectors of the form $(\xi, \zeta, 0)$ and there are four RUMs along the $[0, 0, \xi]^\star$ line as shown by the vertical (red) lines. The new feature uncovered by this search is the undulating surface between the $(\xi, \zeta, 0)$ and $(\xi, \zeta, \frac{1}{2})$ planes, as seen in LHP tridymite (figure 2).

Electron diffraction measurements have sampled the $(\xi, \zeta, 0)$ RUM plane 'edge-on' as streaks of diffuse scattering parallel to the $[\xi, 0, 0]^\star$ and $[\xi, \xi, 0]^\star$ directions. For example, diffraction patterns of natural kalsilite, annealed at around 1200 K detected streaks of diffuse scattering in the $(\xi, \zeta, 0)$ plane parallel to the $[\xi, 0, 0]^\star$ direction [18]. A synthetic sample of kalsilite showed streaking in the same plane, parallel to the $[\xi, \xi, 0]^\star$ direction, as well as parallel to $[\xi, 0, 0]^\star$. In addition, there was streaking along the $[0, 0, \xi]^\star$ line. Other synthetic samples of kalsilite, containing small quantities of sodium substituted for potassium, showed diffuse streaking in the $(\xi, \zeta, 0)$ plane parallel to both $[\xi, 0, 0]^\star$ and $[\xi, \xi, 0]^\star$. In these samples it was found that the intensity of the streaking increased with the sodium concentration. This would be consistent with the smaller size of the sodium cations compared with the potassium cations allowing a larger amplitude of oscillation for the RUMs.

4.2. Nepheline, $Na_3(K, Na)[Al_4Si_4O_{16}]$

The crystal structure of nepheline is another distortion of the basic tridymite structure, albeit not one that is seen in the tridymite polymorphs discussed in this paper. The RUM distribution for nepheline is shown in figure 8. The (red) plane covering the bottom of the box in figure 7 shows that there are four RUMs for all wavevectors of the form $(\xi, \zeta, 0)$. The only other previously discovered feature in this RUM distribution is the existence of two RUMs at $(\frac{1}{3}, \frac{1}{3}, \frac{1}{2})$, e.g. the uppermost part of the green region at the top of figure 7. This search uncovered two new RUM structures, but these are very difficult to present in a way which is clear to the viewer. One is a canopy of RUMs, which connects to the $(\xi, \zeta, 0)$ plane at $(0, 0, 0)$ and $(0, 1, 0)$ in figure 7, and above this there is an undulating surface of a single RUM, which can be seen to graze the $(\xi, \zeta, \frac{1}{2})$ plane, i.e. the top surface of the box, at $(\frac{1}{3}, \frac{1}{3}, \frac{1}{2})$, where the green patches are.

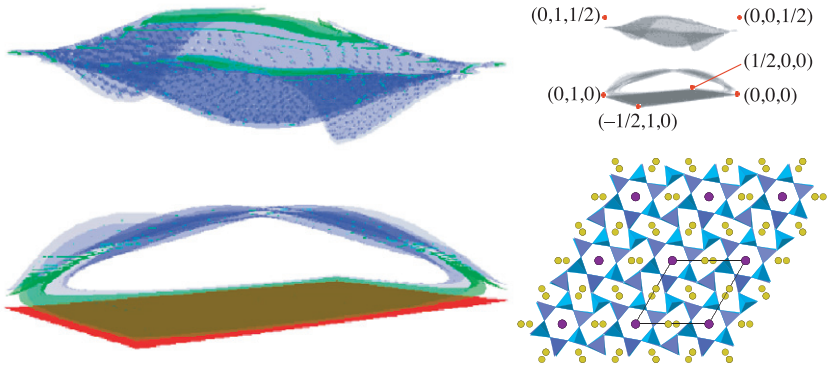

Figure 7. The distribution of RUM wavevectors in a section of reciprocal space for nepheline (the on-line version uses the colour code given in table 1). The upper small inset shows labels of specific points in reciprocal space to aid interpretation. The lower small inset shows a representation of the crystal structure; the space group for this phase is $P6_3$.

These two features are actually connected in the (ξ, ξ, ζ) planes, e.g. the plane which forms the long side face of the box. However, the blue boundary was defined at a higher than usual value of intensity in figure 7, permitting a clearer view into and through the middle of the box. The loci of RUM wavevectors in this plane, which corresponds to the $\langle 1, \overline{1}, 0\rangle$ zone, is shown in figure 8. The bottom right-hand quadrant of the rectangle is equivalent to the long side face of the box in figure 7. The left and right vertices of the diamond in the centre of the section shown in figure 8 are symmetrically equivalent to the $(\frac{1}{3}, \frac{1}{3}, \frac{1}{2})$ position, where there are two RUMs.

There are marked similarities with the same zone section for HP tridymite, also shown in figure 8, which is the parent structure of the nepheline framework. The unit cell of nepheline is doubled along the **a** and **b** axes with respect to the HP phase, but has the same length as the **c** axis. Therefore, the $\mathbf{a}^\star$ and $\mathbf{b}^\star$ reciprocal lattice vectors in nepheline are halved in length compared with HP tridymite. As a result, the section of reciprocal space presented for nepheline corresponds to the left-hand side of the section presented for HP tridymite in figure 8. By translational symmetry, the nepheline reciprocal space section could equally be said to correspond to the right-hand side of the HP tridymite section, and most of the loci in the nepheline pattern may then be obtained as the superposition of the two halves of the HP tridymite pattern.

Single crystal x-ray and electron diffraction studies on nepheline [20, 21, 19] have found peaks of diffuse intensity around $(\frac{1}{3}, \frac{1}{3}, z)$ where $z \approx \pm 0.21$. In most samples investigated a weak streak was found connecting this peak to the adjacent Bragg peak (figure 8). This distribution is similar to features of the calculated curves of RUMs in figure 8. In the calculations, the point corresponding to the experimentally measured diffuse peak is located at $(\frac{1}{3}, \frac{1}{3}, z)$, where $z \approx \pm 0.27$. The intensity of one of these peaks of diffuse scattering was measured using x-ray diffraction (de Dombal, 1991) and the temperature dependence of this intensity was found to follow the equation

$$I \propto \frac{T}{T - T_c} \tag{2}$$

with the transition temperature $T_c = 308$ K. This temperature dependence is characteristic of a phonon in a high symmetry phase softening with lowering temperature to cause a phase transition at T_c to a lower-symmetry phase.

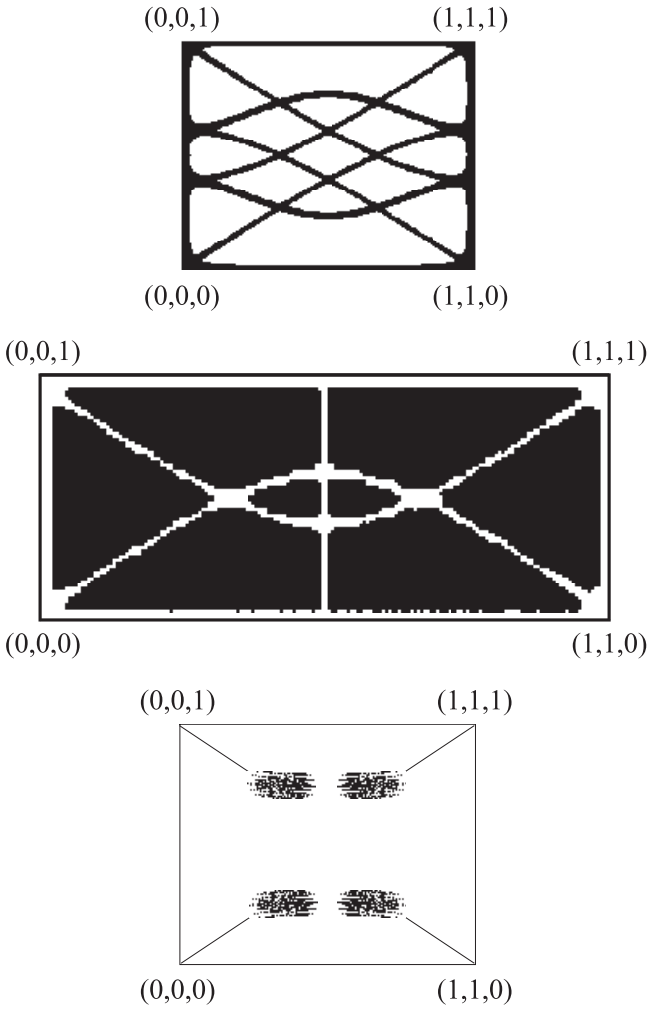

Figure 8. Loci of RUM wavevectors in the $\langle 1, \overline{1}, 0\rangle$ zone axis of nepheline (top) and HP tridymite (centre), and a schematic diagram of diffuse scattering measured in the $\langle 1, \overline{1}, 0\rangle$ zone axis of nepheline (bottom), after McConnell [19].

5. Quartz, SiO_2

5.1. β-quartz

Of all the framework crystals, quartz has probably been studied the most. Thus it is one of the best understood materials, and might not expected to exhibit any unusual behaviour. However, the search for RUMs in β-quartz throughout the whole of the Brillouin zone has shown a new feature, which is shown as the blue undulating web that lies between the top and bottom surfaces of the box in figure 9, i.e. between the planes $(\xi, \zeta, 0)$ and $(\xi, \zeta, \frac{1}{2})$. The figure also clearly illustrates the other RUM features at special wavevectors for β-quartz, as enumerated by Vallade and co-workers [2, 4] and Hammonds *et al* [7].

The vertical (yellow) line to the fore of figure 9 shows three non-degenerate RUMs along the $[0, 0, \xi]^\star$ direction. There is an identical line forming the vertical edge of the box at the

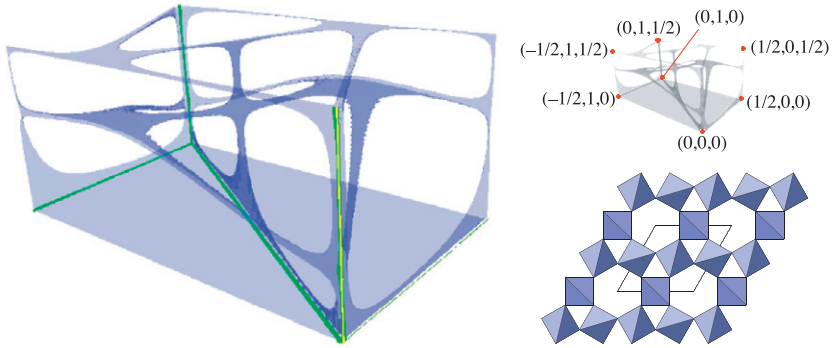

Figure 9. The distribution of RUM wavevectors in a section of reciprocal space for β-quartz (the on-line version uses the colour code given in table 1). The upper small inset shows labels of specific points in reciprocal space to aid interpretation. The lower small inset shows a representation of the crystal structure; the space group for this phase is $P6_222$.

rear of the picture but the yellow core is obscured by the green and blue sheaths surrounding it. The (green) Z-shape on the base of the box shows two non-degenerate RUMs along the $[\xi, 0, 0]^\star$ directions, and the (blue) plane which covers the base of the box represents a single RUM which exists for all wavevectors of the form $(\xi, \zeta, 0)$. The (blue) lines forming the web which zigzags across the top surface of the box indicate a single RUM along the lines $[\xi, \xi, \frac{1}{2}]^\star$ and $[\frac{1}{2} - \xi, 2\xi, \frac{1}{2}]^\star$. The remaining structures are lines of single RUMs along $[\frac{1}{2}, 0, \xi]^\star$: the vertical (blue) lines forming the edges of the box to the left and to the right of the figure as well as the (blue) vertical line in the centre of the box.

The RUMs along the $[\xi, 0, 0]^\star$ directions (the green Z) have been detected experimentally in electron diffraction measurements, which found diffuse intensity in the form of 'astral streaking' radiating out from Bragg peaks along the six $[\xi, 0, 0]^\star$ directions [22]. An inelastic neutron scattering study has determined the phonon dispersion curves of β-quartz [3]. Along $[\xi, 0, 0]^\star$ a soft mode can be seen to mix with one of the transverse acoustic modes, resulting in a branch of phonons whose frequency is less than 1 THz for the whole of the $[\xi, 0, 0]^\star$ line.

5.2. α-quartz

The most notable changes to the RUMs following the α–β phase transition are the disappearance of three RUMs along $[0, 0, \xi]^\star$ and the erosion of the $(\xi, \zeta, 0)$ RUM plane, taking with it the two along $[\xi, 0, 0]^\star$ (figure 10). Some RUMs do remain in this plane, along and close to the $[\xi, \xi, 0]^\star$ lines. Parallel to these, the $[\xi, \xi, \frac{1}{2}]^\star$ lines zigzagging across the top surface of the box, have also remained. The undulating web between the $(\xi, \zeta, 0)$ and $(\xi, \zeta, \frac{1}{2})$ planes, and the $[\frac{1}{2}, 0, \xi]^\star$ lines have also vanished but two new single RUM structures have appeared. These take the form of a snaking line and an almost straight line which both connect the $(\xi, \zeta, 0)$ and $(\xi, \zeta, \frac{1}{2})$ planes.

6. Cristobalite, SiO_2

6.1. β-cristobalite

No new RUM features were found for β-cristobalite, which has a particularly simple distribution of RUM wavevectors. This comprises six intersecting single-RUM planes which

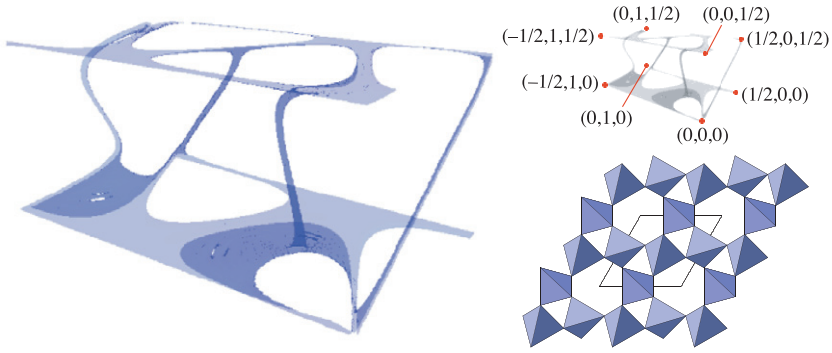

Figure 10. The distribution of RUM wavevectors in a section of reciprocal space for α-quartz (the on-line version uses the colour code given in table 1). The upper small inset shows labels of specific points in reciprocal space to aid interpretation. The lower small inset shows a representation of the crystal structure; the space group for this phase is $P3_121$.

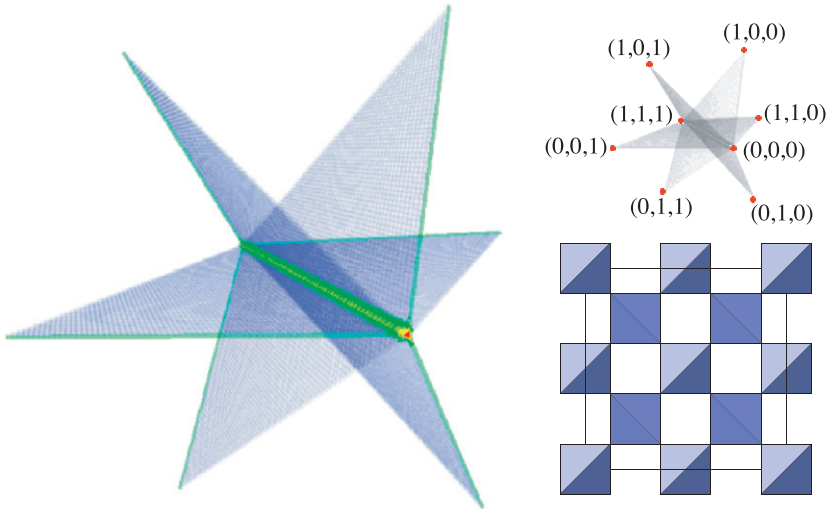

Figure 11. The distribution of RUM wavevectors in a section of reciprocal space for β-cristobalite (the on-line version uses the colour code given in table 1). The upper small inset shows labels of specific points in reciprocal space to aid interpretation. The lower small inset shows a representation of the crystal structure; the space group for this phase is $Fd\bar{3}m$.

are parameterized by (ξ, ξ, ζ), i.e. they are normal to the $\langle 1, \bar{1}, 0\rangle$ directions. The three planes visible in figure 11 (normal to $[1, \bar{1}, 0]$, $[1, 0, \bar{1}]$ and $[0, 1, \bar{1}]$) intersect so as to generate a line of three RUMs along $[\xi, \xi, \xi]^\star$. The three planes not shown (normal to $[1, \bar{1}, 0]$, $[1, 0, \bar{1}]$ and $[0, 1, \bar{1}]$) just graze the axes of the box and they intersect with the visible planes, resulting in the lines of two RUMs along $[\xi, 0, 0]^\star$.

These planes of RUMs in β-cristobalite have been detected experimentally as 'strong diffuse scattering' in electron diffraction measurements [23, 24]. Photographs were taken over temperatures ranging from the transition point at 540 K up to the highest they could reach, which was around 920 K. The diffuse scattering was found to persist with little apparent change over the whole temperature range.

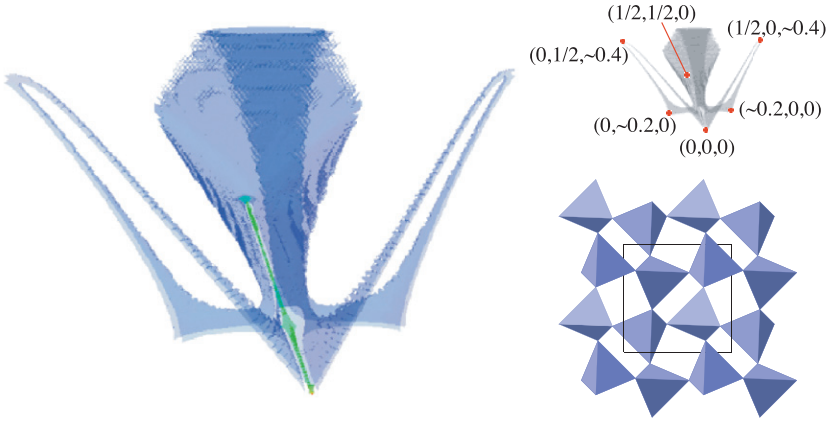

Figure 12. The distribution of RUM wavevectors in a section of reciprocal space for α-cristobalite (the on-line version uses the colour code given in table 1). The upper small inset shows labels of specific points in reciprocal space to aid interpretation. The lower small inset shows a representation of the crystal structure; the space group for this phase is $P4_12_12$.

6.2. α-cristobalite

In contrast to β-cristobalite, the distribution of RUM wavevectors in α-cristobalite is not simple (figure 12). The total number of RUMs for the structure is greatly reduced by the disappearance of the planes of RUMs present in β-cristobalite. There are still two RUMs for general wavevectors along the $[\xi, \xi, 0]^\star$ lines, which correspond to the $[\xi, 0, 0]^\star$ lines in β-cristobalite on transformation of crystallographic axes. However, there are also other, previously undiscovered, RUMs which lie on a strange curved surface and along some curved lines revealed by this search at general wavevectors.

Electron diffraction measurements of α-cristobalite [24] revealed that the diffuse scattering is of a substantially diminished intensity compared with that detected in β-cristobalite. The lines of RUMs along $[\xi, \xi, 0]^\star$ were evident in the photographs (taken at room temperature) but diffuse intensity was also found along $[\xi, 0, 0]^\star$. Phonon dispersion curves for α-cristobalite have been calculated [25] using an empirical interatomic potential model [26]. These showed a low energy mode lying along the $[\xi, 0, 0]^\star$ direction which, whilst not itself a RUM, had been a RUM in β-cristobalite and had not increased drastically in energy. This may account for the diffuse intensity observed along $[\xi, 0, 0]^\star$ in α-cristobalite.

7. Leucite, $KAlSi_2O_6$

7.1. Cubic leucite

For cubic leucite there are four RUMs for general points along the $[\xi, \xi, 0]^\star$ directions, indicated by the (red/dark grey) lines in figure 13, and five RUMs at $(0, 0, 0)$. In addition this search has revealed a rather random and nebulous distribution of wavevectors which have one or two RUMs, the blue and green (light and medium grey) areas, and even some small patches where there are three RUMs (as indicated by the yellow areas).

Experimental evidence of RUMs at the zone centre derives from single crystal x-ray diffraction [27, 28], electron diffraction measurements [29] and inelastic neutron scattering [30] which all measured diffuse scattering at the positions of systematic absences. This scattering increased in intensity as the transition temperature, T_c, was approached from above [27] and

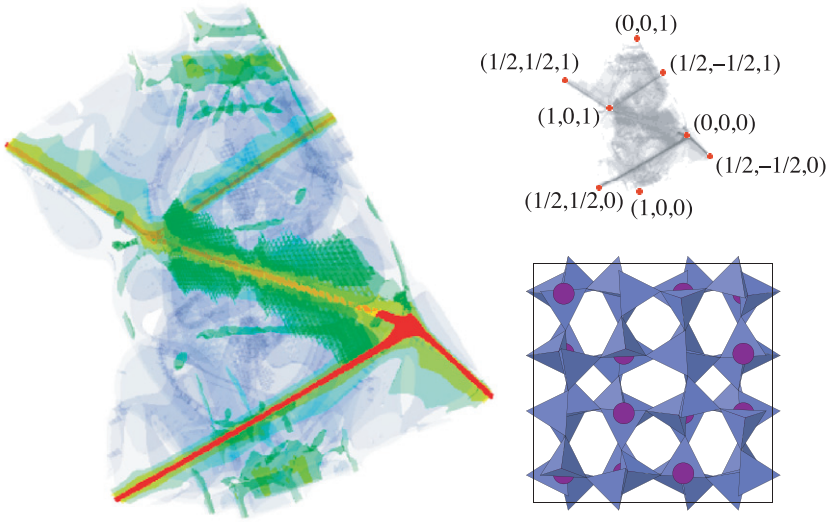

Figure 13. The distribution of RUM wavevectors in a section of reciprocal space for cubic leucite (the on-line version uses the colour code given in table 1). The upper small inset shows labels of specific points in reciprocal space to aid interpretation. The lower small inset shows a representation of the crystal structure; the space group for this phase is $Ia\bar{3}d$.

persisted for temperatures up to 150 or 200 K above [29, 28]. Diffuse intensity at $(\frac{1}{2}, \frac{1}{2}, 0)$ was detected in both the x-ray and neutron experiments, and found to increase in intensity as T_c was approached from above and then vanish below T_c [30, 27]. Additionally, the inelastic neutron scattering was able to detect three low-lying branches along the whole of the line in the dispersion curve for cubic leucite [30] which were interpreted as RUMs by [9].

7.2. Tetragonal leucite

Following the phase transition from cubic to tetragonal leucite, the lines of RUMs disappear [7], but some of the nebulous distribution of RUM wavevectors present in cubic leucite, discovered by this study, remains. This includes a few patches where there are two RUMs, indicated, for example, by the small green areas midway between (0, 0, 0) and (1, 0, 1), i.e. around $(\frac{1}{2}, 0, \frac{1}{2})$ (figure 14). The only wavevectors for which there are three RUMs are for those very close to (0, 0, 0).

8. Cordierite, $Mg_2[Al_4Si_5O_{18}]$

The earlier RUM search at special wavevectors [7] revealed six RUMs for wavevectors of the form $(\xi, \zeta, 0)$, represented by the (red/dark grey) plane, and six RUMs along $[0, 0, \xi]^\star$, the (red/dark grey) vertical lines along the edge of the box in the foreground and background of figure 15. The other feature reported was the existence of two RUMs for wavevectors of the form $(\frac{1}{2}, 0, \xi)$, indicated by the (green/medium grey) lines along the vertical edges of the box to the left and to the right of the picture and the (green/medium grey) vertical line in the centre of the box. This new search has found that there is at least one RUM for almost all general wavevectors. The (blue/lighter grey) surface forms a boundary between the wavevectors where there the number of RUMs is zero or one, and so the regions which appear to be enclosed by the blue crucible-shaped surfaces are in fact the only ones where there are no RUMs.

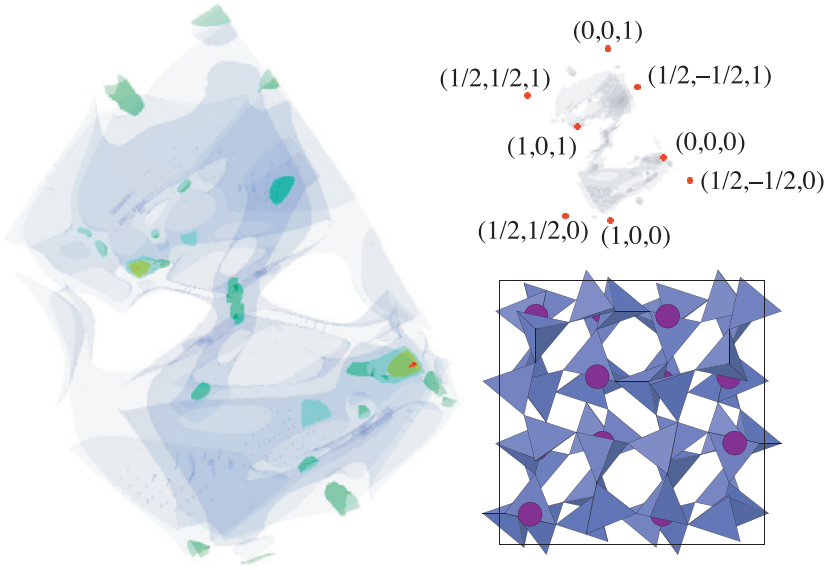

Figure 14. The distribution of RUM wavevectors in a section of reciprocal space for tetragonal leucite (the on-line version uses the colour code given in table 1). The upper small inset shows labels of specific points in reciprocal space to aid interpretation. The lower small inset shows a representation of the crystal structure; the space group for this phase is $I4_1/a$.

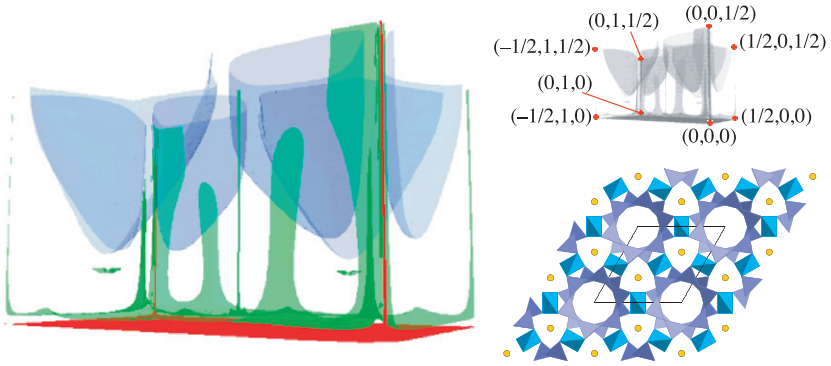

Figure 15. The distribution of RUM wavevectors in a section of reciprocal space for cordierite (the on-line version uses the colour code given in table 1). The upper small inset shows labels of specific points in reciprocal space to aid interpretation. The lower small inset shows a representation of the crystal structure; the space group for this phase is $P6/mcc$.

9. Sodalite, e.g. $Na_8[Al_xSi_{6-x}O_{24}]Cl_2$

9.1. $I\bar{4}3m$ sodalite

There is at least one RUM at every wavevector for $I\bar{4}3m$ sodalite [7], and so the blue surface is not visible in figure 16, since it defines the boundary between wavevectors where the number of RUMs is zero or one. The extreme (yellow) lines, although of varying thickness along their length, indicate the existence of two RUMs for wavevectors of the form $[0, 0, \xi]^\star$. If these lines are considered to form a rather rectangular U-shape then it is easier to see the (green) H-shape

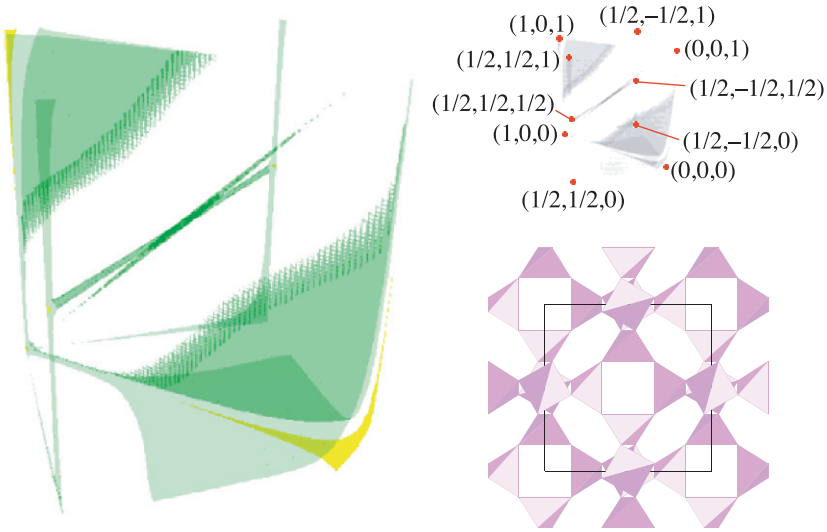

Figure 16. The distribution of RUM wavevectors in a section of reciprocal space for $I\bar{4}3m$ sodalite.

which straddles the U at right angles to it. This H-shape is composed of lines of the form $[\frac{1}{2}, \frac{1}{2}, \xi]^\star$, for which there are two RUMs. There are a couple of (green) lines joining the feet of the H-shape, at $(\frac{1}{2}, \frac{1}{2}, 0)$ and $(\frac{1}{2}, -\frac{1}{2}, 0)$, to one of the corners in the square U-shape, $(1, 1, 0)$. These lines of two RUMs have the form $[\xi, 1-\xi, 0]^\star$ as does the remaining line, a green javelin shape passing through the mid-point of the H-shape. There are three RUMs at $(\frac{1}{2}, \frac{1}{2}, \frac{1}{2})$ as seen from the (yellow) spot half way up the side of the H-shape. All of these features were revealed by the search at special wavevectors. The new information provided by this study derives from the green surfaces surrounding the yellow lines of three RUMs. These (green) 'fins' reveal how slowly the frequency of the middle RUM increases on moving away from these RUM lines.

9.2. $P\bar{4}3n$ sodalite

Since $P\bar{4}3n$ sodalite has a primitive cubic lattice, only one octant of the Brillouin zone is shown in figure 17. When these octants are stacked together to form the whole Brillouin zone it can be seen that the red lines form part of two interlocking, but non-intersecting, cubic frameworks. For these wavevectors there are four RUMs, except at the intersections where there are six RUMs. This structure is equivalent to the set of RUMs revealed by the search at special wavevectors [7]. This study shows that, in addition, this phase of sodalite has at least one RUM for almost all wavevectors, and so the blue curved surfaces, together with the sides of the box, enclose the small regions of reciprocal space where there are no RUMs (figure 17). Since these RUMs are not found at every general wavevector, this feature is not listed by Hammonds *et al* [7].

10. Discussion

10.1. General observations

Performing searches for RUMs at general rather than just special wavevectors has revealed a surprising number of previously unknown distributions of RUMs in the reciprocal space

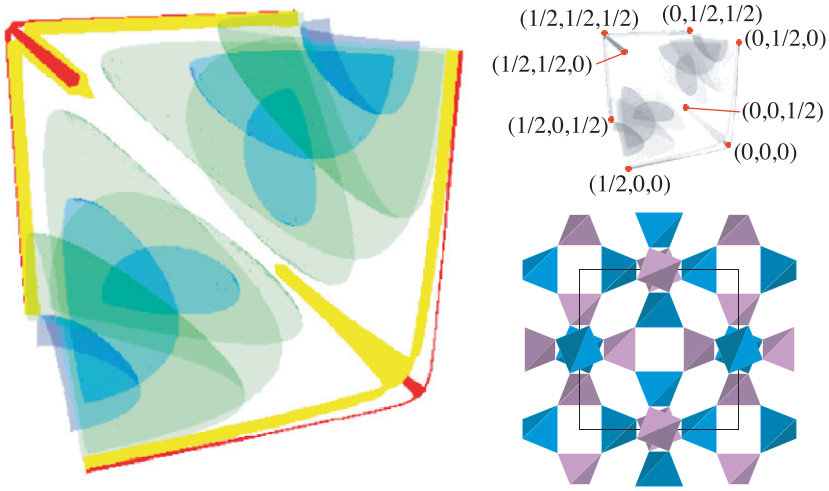

Figure 17. The distribution of RUM wavevectors in a section of reciprocal space for $P\bar{4}3n$ sodalite.

of a variety of framework silicates and aluminosilicates. These distributions take the form of intriguing curves and surfaces of wavevectors, and they are surprisingly common, even amongst the lower-symmetry phases. These results have changed our understanding of RUMs in framework crystals in two respects. *Firstly*, the distribution of RUMs in reciprocal space can comprise a much more complicated set of wavevectors than simply those with special symmetries. *Secondly*, the number of RUMs in these crystals is greater than was previously thought to be the case, and this is particularly noticeable amongst lower-symmetry phases, since they have fewer RUMs at special wavevectors than their higher-symmetry counterparts.

The complexity of the RUM distributions changes the question of how we should understand the origin of RUMs. RUMs arise when there are degeneracies in the structural constraints on the crystal framework, and these degeneracies depend upon the crystal symmetry. The picture that emerges is that this degeneracy due to symmetry does not necessarily have a simple dependence upon wavevector, and it turns out that it can be quite complicated. Why this should be so is an interesting and non-trivial question.

It is probable that the origin of exotic surfaces of RUMs in the crystalline phases is not disconnected from the origin on RUMs in amorphous silica [33], where there is no symmetry that will generate degeneracies amongst the structural constraints.

The surprisingly high occurrence of RUMs at general wavevectors may be considered from the perspective of the roles played by RUMs as soft modes in displacive phase transitions. Although all RUMs are potential candidates for soft modes, in practice only RUMs at special symmetry points, or along symmetry lines, soften to precipitate displacive phase transitions; incommensurate phase transitions are not common even though there are many incommensurate RUMs. Thus, in the case of higher-symmetry phases it is found that a RUM at a special wavevector will soften in preference to a RUM at a general wavevector. Then, in the case of the lowest-symmetry phase of a crystal, no phonon modes soften, despite the existence of these RUMs. These observations raise the question of why the RUMs on these complicated surfaces of wavevectors are apparently so unfavourable as soft modes.

RUMs also play the role of mediators of dynamic disorder in crystals. This has been studied in some detail for cristobalite, quartz and ZrW_2O_8 using both RUM theory and neutron

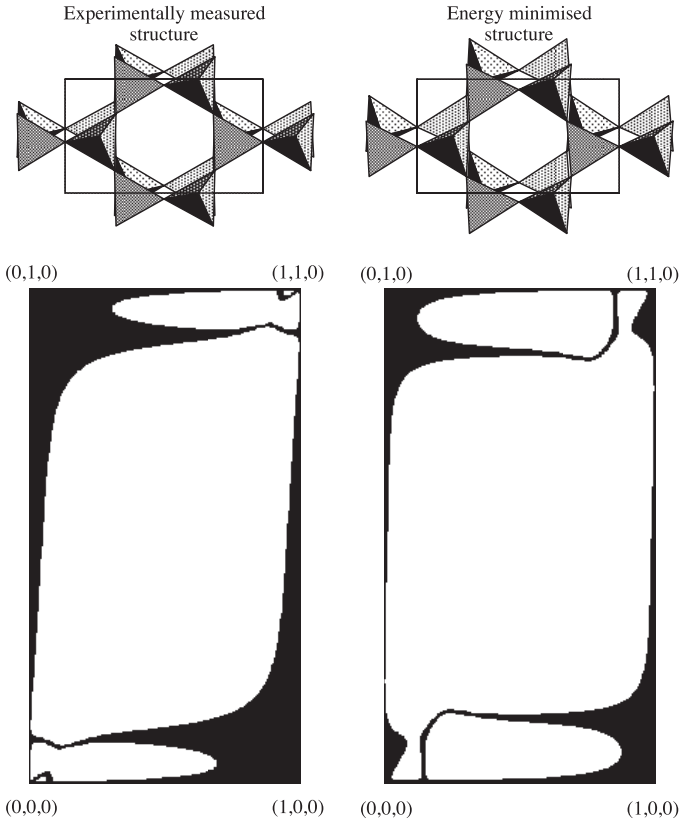

Figure 18. The crystal structures and RUM wavevector distribution in the $(\xi, \zeta, 0)$ plane for the experimentally determined OC tridymite structure and an energy minimized version of the same structure.

total scattering experiments [34–37], the latter being of particular interest with regard to understanding the role of RUMs in negative thermal expansion. The point emerging from this study is that there are significantly more RUMs on general wavevectors than had previously been appreciated, and thus the role of RUMs in generating dynamic disorder is now seen to be greater than previously understood.

10.2. The sensitivity of RUM wavevector distributions to symmetry-conserving changes in the crystal structure

Distributions of RUMs in reciprocal space can and do comprise both special symmetry wavevectors and general wavevectors. It is likely that the location of the RUMs at special wavevectors will follow directly from the crystal topology and symmetry. However, the exact location of RUMs at general wavevectors may be less fixed, and these distributions might therefore be sensitive to subtle perturbations of the crystal structure, which do not alter the space group symmetry.

The OC phase of tridymite was used to investigate this possibility. For this phase, the $(\xi, \zeta, 0)$ plane in reciprocal space was earlier shown to contain RUMs along a mixture of special lines, $[\xi, 0, 0]^\star$ and $[0, \zeta, 0]^\star$, and general curves, and so this plane provides a suitable test case.

Using the experimental structure refinement [31] as a starting point, the crystal structure of OC tridymite was relaxed by performing a symmetry-constrained lattice energy minimization using the code GULP [32] with the empirical interatomic potential model of Sanders *et al* [26]. The experimentally measured and energy minimized structures are compared in figure 18, together with the corresponding distributions of RUM wavevectors in the $(\xi, \zeta, 0)$ plane.

In real space, the amplitude of the deviation from the ideal crystal structure of HP tridymite is noticeably greater in the relaxed structure than in the measured one, since it comprises larger translations and rotations of the SiO_4 tetrahedra. Following these changes in crystal structure, the location of the RUMs along the $[\xi, 0, 0]^\star$ and $[0, \zeta, 0]^\star$ lines in reciprocal space remains unaltered, as expected. The surprising result is the change in the structure of the RUM wavevector loci at general wavevectors, which actually involve a change in their topology. The feature of RUM lines branching off the symmetry lines remains, subject to changes in the exact position of the branching point, but the manner in which these branches connect to each other has altered. As a result, the bow-tie-shaped locus centred on the zone centre in the experimental structures distribution is not present in the relaxed structures distribution of RUM wavevectors. This simple set of calculations demonstrates that within a specific topology and even a specific symmetry for a framework structure, the wavevectors for which zero-energy modes of deformation exist can vary significantly.

Acknowledgment

We acknowledge funding from NERC.

References

[1] Grimm H and Dorner B 1975 Mechanism of α–β phase transformation of quartz *J. Phys. Chem. Solids* **36** 407–13
[2] Berge B, Bachheimer J P, Dolino J, Vallade M and Zeyen C 1986 Inelastic neutron scattering study of quartz near the incommensurate phase transition *Ferroelectrics* **66** 73–84
[3] Dolino G, Berge B, Vallade M and Moussa F 1992 Origin of the incommensurate phase of quartz: I. Inelastic neutron scattering study of the high temperature α phase of quartz *J. Physique* I **2** 1461–80
[4] Vallade M, Berge B and Dolino G 1992 Origin of the incommensurate phase of quartz: II. Interpretation of inelastic neutron scattering data *J. Physique* I **2** 1481–95
[5] Dove M T, Giddy A P and Heine V 1991 Rigid unit mode model of displacive phase transitions in framework silicates *Trans. Am. Crystallogr. Assoc.* **27** 65–75
[6] Giddy A P, Dove M T, Pawley G S and Heine V 1993 The determination of rigid unit modes as potential soft modes for displacive phase transitions in framework crystal structures *Acta Crystallogr.* A **49** 697–703
[7] Hammonds K D, Dove M T, Giddy A P, Heine V and Winkler B 1996 Rigid unit phonon modes and structural phase transitions in framework silicates *Am. Mineral.* **81** 1057–79
[8] Hammonds K D, Dove M T, Giddy A P and Heine V 1994 CRUSH: a FORTRAN program for the analysis of the rigid unit mode spectrum of a framework structure *Am. Mineral.* **79** 1207–9
[9] Dove M T, Heine V and Hammonds K D 1995b Rigid unit modes in framework silicates *Mineral. Mag.* **59** 629–39
[10] Hammonds K D, Bosenick A, Dove M T and Heine V 1998 Rigid unit modes in crystal structures with octahedrally-coordinated atoms *Am. Mineral.* **83** 476–9
[11] Thorpe M F 1983 Continuous deformations in random networks *J. Non-Cryst. Solids* **57** 355–70
[12] He H and Thorpe M F 1985 Elastic properties of glasses *Phys. Rev. Lett.* **54** 2107–10
[13] Phillips J C and Thorpe M F 1985 Constraint theory, vector percolation and glass formation *Solid State Commun.* **53** 699–702
[14] Withers R L, Thompson J G, Xiao Y and Kirkpatrick R J 1994 An electron diffraction study of the polymorphs of SiO_2-tridymite *Phys. Chem. Minerals* **21** 421–33
[15] Dove M T, Hammonds K D, Heine V, Withers R L, Xiao Y and Kirkpatrick R J 1995 Rigid unit modes in the high-temperature phase of SiO_2 tridymite: calculations and electron diffraction *Phys. Chem. Minerals* **23** 56–62

[16] Pryde A K A, Hammonds K D, Dove M T, Heine V, Gale J D and Warren M C 1996 Origin of the negative thermal expansion in ZrW_2O_8 and ZrV_2O_7 *J. Phys.: Condens. Matter* **8** 10973–82
[17] Dove M T 1993 *Introduction to Lattice Dynamics* (Cambridge: Cambridge University Press)
[18] Xu H and Veblen D R 1996 Superstructures and domain structures in natural and synthetic kalsilite *Am. Mineral.* **81** 1360–70
[19] McConnell J D C 1961 Electron-diffraction study of subsidiary maxima of scattered intensity in nepheline *Mineral. Mag.* **32** 114–24
[20] de Dombal R F 1991 Phase transitions in the nepheline–kalsilite solid solution *PhD Thesis* University of Cambridge
[21] Hayward S A, Pryde A K A, de Dombal R F, Carpenter M A and Dove M T 2000 Rigid unit modes in disordered nepheline: a study of a displacive incommensuate phase transition *Phys. Chem. Minerals* **27** 285–90
[22] Heaney P J and Veblen D R 1991 Observations of the α–β phase transition in quartz: a review of imaging and diffraction studies and some new results *Am. Mineral.* **76** 1018–32
[23] Hua G L, Welberry T R, Withers R L and Thompson J G 1988 An electron diffraction and lattice-dynamical study of the diffuse scattering in β-cristobalite, SiO_2 *J. Appl. Crystallogr.* **21** 458–65
[24] Withers R L, Thompson J G and Welberry T R 1989 The structure and microstructure of α-cristobalite and its relationship to β-cristobalite *Phys. Chem. Minerals* **16** 517–23
[25] Dove M T, Harris M J, Hannon A C, Parker J M, Swainson I P and Gambhir M 1997 Floppy modes in crystalline and amorphous silicates *Phys. Rev. Lett.* **78** 1070–3
[26] Sanders M J, Leslie M and Catlow C R A 1984 Interatomic potentials for SiO_2 *J. Chem. Soc. Chem. Commun.* 1271–3
[27] Palmer D C and Salje E K H 1990 Phase transitions in leucite: dielectric properties and transition mechanism *Phys. Chem. Minerals* **17** 444–52
[28] Palmer D C, Salje E K H and Schmahl W W 1989 Phase transitions in leucite: x-ray diffraction studies *Phys. Chem. Minerals* **16** 714–9
[29] Heaney P J and Veblen D R 1990 A high-temperature study of the low–high leucite phase transition using the transmission electron microscope *Am. Mineral.* **75** 464–76
[30] Boysen H 1990 Neutron scattering and phase transitions in leucite *Ferroelastic and Co-elastic Crystals* ed E K H Salje (Cambridge: Cambridge University Press) pp 334–47
[31] Dollase W A 1967 The crystal structure at 220 °C of orthorhombic high tridymite from the Steinbach meteorite *Acta Crystallogr.* **23** 617–23
[32] Gale J D 1997 GULP: a computer program for the symmetry-adapted simulation of solids *J. Chem. Soc.: Faraday Trans.* **93** 629–37
[33] Trachenko K O, Dove M T, Harris M J and Heine V 2000 Dynamics of silica glass: two-level tunneling states and low-energy floppy modes *J. Phys.: Condens. Matter* **12** 8041–64
[34] Tucker M G, Squires M D, Dove M T and Keen D A 2001 Dynamic structural disorder in cristobalite: neutron total scattering measurement and reverse Monte Carlo modelling *J. Phys.: Condens. Matter* **13** 403–23
[35] Tucker M G, Dove M T and Keen D A 2000 Simultaneous analyses of changes in long-range and short-range structural order at the displacive phase transition in quartz *J. Phys.: Condens. Matter* **12** L723–30
[36] Wells S A, Dove M T, Tucker M G and Trachenko K O 2002 Real-space rigid unit mode analysis of dynamic disorder in quartz, cristobalite and amorphous silica *J. Phys.: Condens. Matter* **14** 4645–57
[37] Tucker M G, Goodwin A L, Dove M T, Keen D A, Wells S A and Evans J S O 2005 Negative thermal expansion in ZrW_2O_8: mechanisms, rigid unit modes, and neutron total scattering *Phys. Rev. Lett.* **95** 255501